Active power dispatch for supporting grid frequency regulation in wind farms considering fatigue load

Liu, Yingming; Wang, Yingwei; Wang, Xiaodong; Zhu, Jiangsheng; Lio, Wai Hou

Published in:
Energies

Link to article, DOI:
10.3390/en12081508

Publication date:
2019

Document Version
Publisher's PDF, also known as Version of record

energies

MDPI

Article

Active Power Dispatch for Supporting Grid Frequency Regulation in Wind Farms Considering Fatigue Load

Yingming Liu [1], Yingwei Wang [1,*], Xiaodong Wang [1], Jiangsheng Zhu [2] and Wai Hou Lio [3]

[1] Institute of Electrical Engineering, Shenyang University of Technology, Shenyang 110870, China; yingming.liu@hrwind.com (Y.L.); xiaodong.wang@hrwind.com (X.W.)
[2] Energy Department of Technology, Aalborg University, 6700 Esbjerg, Denmark; jzh@et.aau.dk
[3] Department of Wind Energy, Technical University of Denmark, 4000 Roskilde, Denmark; wali@dtu.dk
* Correspondence: yingwei.wang@hrwind.com; Tel.: +86-024-25670358

Received: 28 February 2019; Accepted: 17 April 2019; Published: 21 April 2019

Abstract: This paper proposes an active power control method for supporting grid frequency regulation in wind farms (WF) considering improved fatigue load sensitivity of wind turbines (WT). The control method is concluded into two parts: frequency adjustment control (FAC) and power reference dispatch (PRD). On one hand, the proposed Fuzzy-PID control method can actively maintain the balance between power generation and grid load, by which the grid frequency is regulated when plenty of winds are available. The fast power response can be provided and frequency error can be reduced by the proposed method. On the other hand, the sensitivity of the WT fatigue loads to the power references is improved. The explicit analytical equations of the fatigue load sensitivity are re-derived to improve calculation accuracy. In the process of the optimization dispatch, the re-defined fatigue load sensitivity will be used to minimize fatigue load. Case studies were conducted with a WF under different grid loads and turbulent wind with different intensities. By comparing the frequency response of the WF, rainflow cycle, and Damage Equivalent Load (DEL) of the WT, the efficacy of the proposed method is verified.

Keywords: fatigue load; active power dispatch; frequency regulation; fuzzy control; wind farm

1. Introduction

Wind energy is one of the rapidly growing renewable energy sources [1–4]. By far largest wind power market, China installed an additional capacity of 19 Gigawatts, and continues its undisputed position as the world's wind power leader [5–8]. With the rapid growth of installed wind power capacity, its proportion in the power grid continues to increase. Wind power generally does not participate in frequency regulation due to the decoupling of the WT rotor and the grid frequency, so large-scale wind power access to the grid will significantly weaken the frequency regulation capability of the grid [9,10]. With the continuous increase of the wind power penetration rate, the influence of wind power volatility and uncertainty on the frequency regulation of power systems is also increasing [11–15]. In order to meet grid frequency requirements, active power control (APC) method for wind power is critical to actively maintaining a balance between power generation. However, the power reference is frequently changed by the FAC to adapt to changes in the grid frequency when the WF participates in frequency regulation. The frequent action of the pitch angle of the WT and the torque of the generator is caused by this change, resulting in an increase in the fatigue loads of WTs [16–19]. Therefore, it is necessary to study which control methods support grid frequency regulation without affecting or even reducing the fatigue loads of WTs.

In recent research, some methods for supporting grid frequency regulation have been proposed. An approach for participation of doubly fed induction generator (DFIG) based wind farms in power

system short-term frequency regulation to simplify the high-order average frequency models of bulk power systems was proposed in [20,21]. In [22,23], the inertia constant and primary power reserve for a variable speed wind turbine that operates at derated conditions were formulated in a wind farm to support short-term frequency control in power systems. Reference [24] presents a model-based control method based on Model Predictive Control (MPC) method and on a Kalman-like estimation algorithm to improve the contribution of wind power generators to short-time primary frequency regulation in electric power systems. A frequency control support function responding proportionally to frequency deviation is proposed to take out the kinetic energy of wind turbine for improving the frequency response of the system in reference [25]. However, the grid frequency is only stabilized in a short period of time using these methods. Reference [26] presented two APC methods that are developed based on adaptive pole placement control (APPC) and fuzzy proportional-integral (PI) control approaches to provide rapid power response. The grid frequency can be stabilized for a long time by WF power reduction. However, it can be seen from the DELs results that the fatigue load of WT has been increased using this method. For wind farm power distribution, as long as the power scheduling requirements are met, the fatigue load can be minimized by coordination between the WTs [27]. In [28,29], a distributed MPC based APC method of WFs was presented to reduce the fatigue loads of WTs. In [30], a load sensitivity based optimal active power dispatch algorithm is proposed for wind farms. The explicit analytical equations of the load sensitivity are derived to improve the computational efficiency of controller. Two fatigue loads experienced by shaft torque and tower bending moment are considered.

An APC method is proposed in this paper. This method is used to provide fast power response while minimizing fatigue loading on the WT, which is used to overcome the above problems. The frequency adjustment control of WF was developed based on the Fuzzy-PID control method. The method is designed to track various forms of load while maintaining grid frequency stability when plenty of wind is available. The total active power obtained by the FAC is proportionally distributed to the wind farms. The fast power response can be provided and frequency error can be reduced by the proposed method compared with traditional methods. Based on the resulting power reference value, the PRD adjusts the power reference of WT within the WF to track power. The model of the WT is improved and the analytical equation for fatigue load sensitivity is re-derived. Compared with the original method, the calculation accuracy is improved by the improved method. Meanwhile, PRD minimizes fatigue loads of tower thrust and shaft torque variations based on the improved fatigue load sensitivity model. Following this, a complete system simulation model is built in MATLAB to verify the effectiveness of the proposed method.

The main contributions of this work are described as follows: A control structure support frequency adjustment for large-scale WF is proposed in Section 2. Section 3 designs a Fuzzy-PID controller to respond and recover grid frequencies more quickly. The fatigue load sensitivity model of the wind turbine is improved and the explicit analytical equations of the fatigue load sensitivity are re-derived in Section 4. The improved model can adapt to wind conditions with different turbulence intensity to minimize the shaft torque and tower bending moment fatigue loads. The simulation results demonstrate the effectiveness of the method in Section 5. Section 6 concludes the paper.

2. Control Structure of WF Participates in Frequency Regulation

The proposed WF control architecture proposed in the paper is shown in Figure 1. The control architecture is mainly divided into two parts.

The first part is FAC of the WF. The measured grid frequency f_{meas} is used as a feedback signal to set up active power control in real-time and maintain the balance between power generation and grid loads. The demanded power of WF $P_{\text{demand}}^{\text{WF}}$ is calculated by FAC and delivered to the PRD. The grid frequency is regulated by FAC to its rated value despite a changing grid load. The second part is PRD of the WF. This part takes all the WTs as the unit and performs power tracking on the power value assigned by the superior to realize the active power adjustment of the WT in the area under his

jurisdiction. The fatigue load sensitivity $\frac{\partial L}{\partial P^{WT}_{demand}}$ is calculated by PRD using a and b obtained by the wind turbine generator (WTG) controller. The details of $\frac{\partial L}{\partial P^{WT}_{demand}}$, a and b are described in Section 4. Then the local WTG controller does not need to be changed.

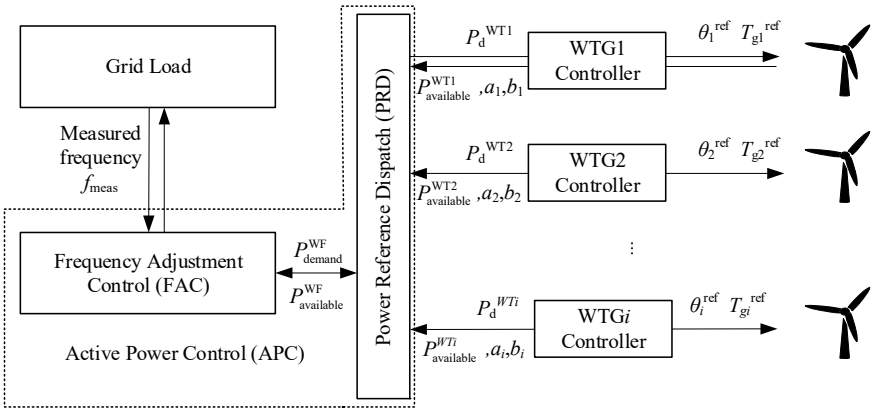

Figure 1. Architecture of active power control for WF.

3. Fuzzy-PID Control Method of Supporting Grid Frequency Regulation for WF

The frequency fluctuation of the power system is caused by the imbalance of the generation and consumption of active power. In order to maintain the frequency stability of the power system, the system frequency must be maintained by active power control. The greater the balance between power generation and consumption, the smaller the frequency fluctuations, and the higher the electricity quality. This paper considers active power control at an entire WF level within the general structure shown in Figure 1. A typical large-scale WF including N wind turbines is included.

When the penetration of wind power in the power grid is relatively low, the impact of wind power participation in frequency regulation is minimal, so the wind farm frequency regulation method uses open-loop control. However, with the increase of wind power penetration rate, this open-loop control method cannot adapt to this situation and will cause the frequency to produce steady-state error. Traditional proportion-integral-derivative (PID) controllers are one of the most widely used controllers in industrial applications, and they can eliminate the steady-state error of the frequency [31–33]. However, it is difficult to adapt to a wind power conversion system with strong nonlinear dynamic characteristics, which needs to be improved.

The fuzzy control system establishes a fuzzy rule table suitable for the actual production process by summarizing expert knowledge and operational experience. It not only reduces the rise time and overshoot of the output response, but also reduces the sensitivity of the system to interference and increases the stability of the system [34]. Fuzzy-PID can adjust the size of the parameters for P, I, and D online, and it can adapt well to dynamic systems [35,36]. In this paper, the Fuzzy-PID controller is used to regulate the grid frequency. In the APC architecture proposed in this paper, the input of the fuzzy controller is the frequency deviation f_{error} of the grid, and the output is the demanded power of WF P^{WF}_{demand}. The demanded power is then sent to PRD.

As it is shown in Figure 2, grid frequency error f_{error} is calculated by

$$f_{error} = f_{meas} - f_N \quad (1)$$

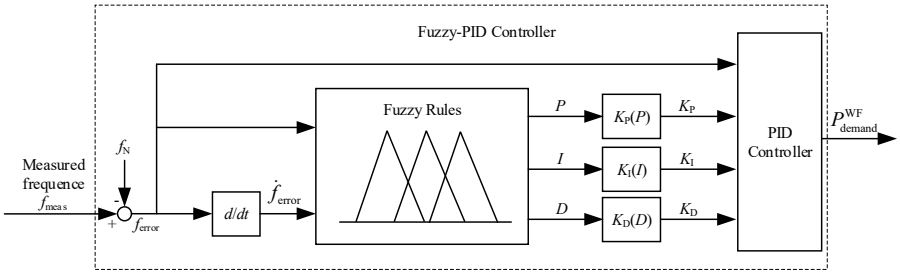

Figure 2. Fuzzy-PID controller.

The APC control method determines the WF power demand $P^{\mathrm{WF}}_{\mathrm{demand}}$ for adjusting the grid frequency through input f_{error}. $\dot{f}_{\mathrm{error}}$ is a nonlinear differential approximation. K_{P}, K_{I} and K_{D} are calculated by

$$K_{\mathrm{P}}(P) = a_{\mathrm{P}}P + b_{\mathrm{P}} \tag{2}$$

$$K_{\mathrm{I}}(I) = a_{\mathrm{I}}I + b_{\mathrm{I}} \tag{3}$$

$$K_{\mathrm{D}}(D) = a_{\mathrm{D}}D + b_{\mathrm{D}} \tag{4}$$

The constants b_{P}, b_{I}, and b_{D} represent a conventional PID controller that provides a good but not optimum system response. These constants can be obtained using any conventional methods for PID controllers. In (2), (3), and (4), the coefficients a_{P}, a_{I}, and a_{D} are obtained according to simulation results to determine the relevant ranges of variations for b_{P}, b_{I}, and b_{D}, respectively. The parameters of P, I, and D onlines are determined by the fuzzy rules in Figure 3. Membership functions for inputs and outputs are shown in Figure 3. The vertical axes represent the degree of membership that is within the range of [0, +1].

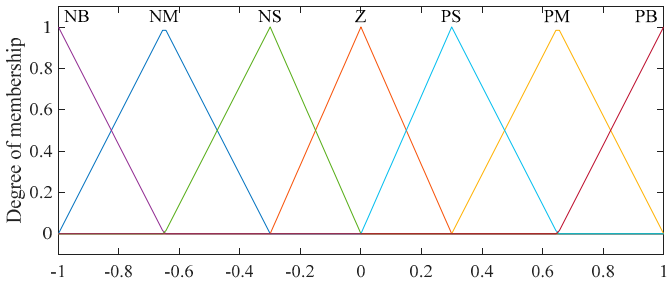

Figure 3. Membership functions for inputs and outputs.

The meaning of the linguistic variables is listed in Table 1.

Table 1. Linguistic variables of membership functions.

Linguistic Variables	Meaning
NB	Negative big
NM	Negative medium
NS	Negative small
Z	Zero
PS	Positive small
PM	Positive medium
PB	Positive big

The input parameters are blurred and then defuzzified, the explicit control signal obtained after defuzzification is shown in Figure 4. Note that the inputs f_{error} and $\dot{f}_{\mathrm{error}}$ of fuzzy rules need to be

normalized within the range [−1, +1] before being processing in Figure 4, where e represents f_{error}; de represents $\dot{f}_{\text{error}}$.

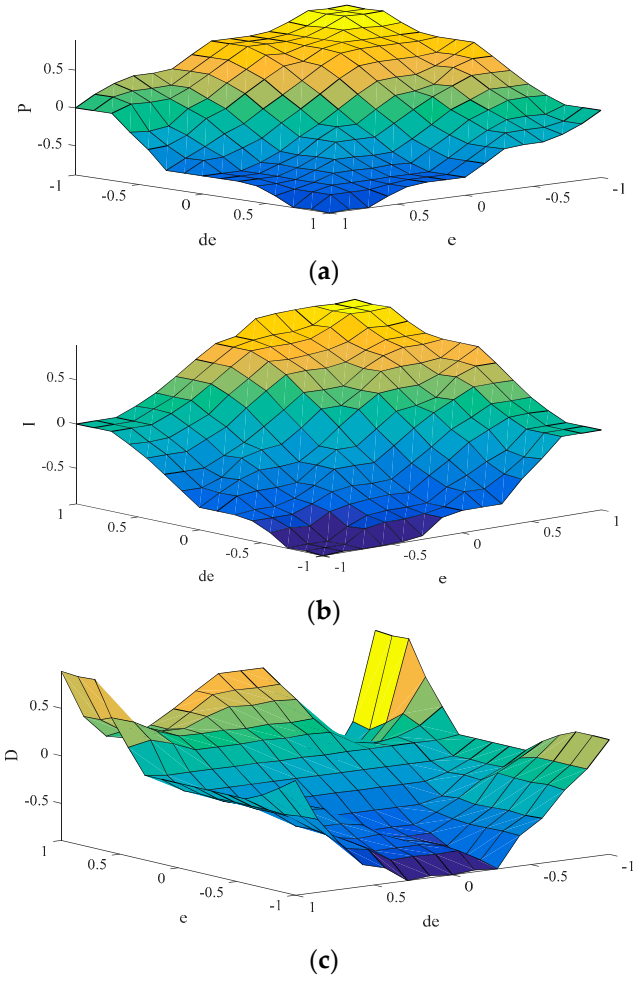

Figure 4. Control signal of P, I and D after defuzzification. (**a**) Control signal of P after defuzzification.; (**b**) Control signal of I after defuzzification.; (**c**) Control signal of D after defuzzification.

4. PRD Method for WT Based on Fatigue Load Sensitivity Using Quadratic Programming Algorithm

In the wind farm power reference dispatch section, the power reference dispatch controller regulates all the WT active outputs of the wind farm. The controller aims to minimize the fatigue load of WT and track the active power allocated by the frequency adjustment controller. Typically, the sampling time of the wind farm controller is in seconds [28]. Therefore, the rapid dynamics of generators and pitch actuators can be ignored [37]. In addition, shaft torsion and tower point oscillations are ignored to reduce the complexity of the model.

The fatigue loads of WTs can be divided into two parts: one is aerodynamic loads and gravity loads (external), and the other is structural loads (internal) [38]. In this paper, the fatigue loads mainly focus on the loads of the drive train due to the torsion of the shaft and the loads of the tower structure due to the tower deflection. Compared with static loads, the dynamic stress causing structural damage of WTs is a much bigger issue. By reducing the fluctuations of low-speed shaft torque T_s and thrust force F_t, the related fatigue loads can be reduced. $\frac{\partial L}{\partial P_{\text{demand}}^{WT}}$ can be represented by a combination of $\frac{\partial T_s}{\partial P_{\text{demand}}^{WT}}$ and $\frac{\partial F_t}{\partial P_{\text{demand}}^{WT}}$ when the drive train and tower structure loads are considered.

4.1. Improved Model of Fatigue Load Sensitivity

The WT (NREL 5 MW) developed by the National Renewable Energy Laboratory (NREL) is used in this paper [39,40]. The oscillations in the shaft torsion and tower nodding are disregarded, the fluctuations of wind speed are ignored based on the previous report [30]. In order to better optimize the calculation, the equations of fatigue load sensitivity are re-derived. In the process of the optimization dispatch, the redefined fatigue load sensitivity will be used. The active power of the WT output is still controlled by adjusting the pitch angle and torque.

The equivalent mass J_t of drive train system is described by [41]

$$J_t = J_r + \eta_g^2 J_g \tag{5}$$

where J_r is the rotor mass; J_g is the generator mass; η_g is the gear box ratio.

The low-shaft motion equation is described by

$$\dot{\omega}_r \approx \frac{1}{J_t}(T_{rot} - \eta_g T_g) \tag{6}$$

where ω_r is the measured rotor speed; T_{rot} is the aerodynamic torque; T_g is the generator torque;

The measured generator speed ω_g is filtered by a low-pass filter and the filtered speed ω_f is

$$\omega_f = \frac{1}{1 + s \cdot \tau_f}\omega_g \tag{7}$$

where τ_f is time constant of the filter of ω_g.

According to the deviation of ω_f from generator rated speed $\omega_{g\text{-rated}}$, pitch angle reference θ_{ref} can be obtained by the PI controller.

$$\theta_{ref} = \frac{1}{k_a}[k_p + \frac{k_i}{s}](\omega_f - \omega_{g-rate}) \tag{8}$$

where k_p is the proportional gain; k_i is the integral gain; k_a is a function of θ_{ref}, defined by $k_a \triangleq k_{a1} + k_{a2}\theta_{ref}$. Where k_{a1} and k_{a2} are the constants.

By defining

$$\beta \triangleq k_a \theta_{ref} \tag{9}$$

(8) is transformed into

$$\beta = k_p(\omega_f - \omega_{g-rate}) + k_i \frac{(\omega_f - \omega_{g-rate})}{s} \tag{10}$$

According to the motion equation of shaft torque T_s, $\dot{\omega_r}$, and $\dot{\omega_g}$ can be described by

$$\dot{\omega}_r \approx \frac{1}{J_r}(T_{rot} - T_s - B(\omega_r - \frac{\omega_g}{\eta_g})) \tag{11}$$

$$\dot{\omega}_g \approx \frac{1}{J_g}(\frac{1}{\eta_g}(T_s + B(\omega_r - \frac{\omega_g}{\eta_g})) - T_g) \tag{12}$$

where ω_g is the measured generator speed; B is the main shaft viscous friction coefficient.

According to (11) and (12), $\dot{\omega_g}$ can be expressed by

$$\dot{\omega}_g \approx \frac{1}{J_g}(\frac{1}{\eta_g}(T_{rot} - J_r\dot{\omega}_r) - T_g) = \frac{1}{J_g}(1 - \frac{J_r}{J_t})(\frac{T_{rot}}{\eta_g} - T_g) \tag{13}$$

The time of the operating point is assumed to be k. The wind speed v is a variable that can be estimated or measured [42]. In this study, v is estimated. The value at $t = k$ is v_0 and is assumed to be constant over a short control period. The measured power output, generator speed, filtered speed,

and pitch angle are defined as P_{g0}, ω_{g0}, ω_{f0}, and θ_0 at $t = k$, respectively. The T_{rot} and T_g at $t = k$ can be defined as T_{rot0} and T_{g0}, respectively.

Based on (6), (7), (10), and (13), the incremental form can be obtained as

$$\Delta\dot{\omega}_r = \frac{1}{J_t}(\Delta T_{rot} - \eta_g \Delta T_g) + \frac{1}{J_t}(T_{rot0} - \eta_g \Delta T_{g0}) \tag{14}$$

$$\Delta\dot{\omega}_f = -\frac{1}{\tau_f}\Delta\omega_f + \frac{1}{\tau_f}\Delta\omega_g \tag{15}$$

$$\Delta\dot{\beta} = \frac{k_p}{\tau_f}\Delta\omega_g + (-\frac{k_p}{\tau_f} + k_i)\Delta\omega_f + k_i(\omega_{f0} - \omega_{g-rate}) \tag{16}$$

$$\Delta\dot{\omega}_g = \frac{1}{J_g}(1 - \frac{J_r}{J_t})(\frac{\Delta T_{rot}}{\eta_g} - \Delta T_g) + \frac{1}{J_g}(1 - \frac{J_r}{J_t})(\frac{T_{rot0}}{\eta_g} - T_{g0}) \tag{17}$$

The aerodynamic torque T_{rot} is calculated by

$$T_{rot} = \frac{0.5\pi R^2 \rho v^3 C_p(\lambda, \theta)}{\omega_r} \tag{18}$$

where R is the length of the blade; ρ is the air density; v is the wind speed on the rotor; C_p is the power coefficient; λ is the tip speed ratio, defined by $\lambda \triangleq \frac{\omega_r R}{v}$; In order to simplify the expression, P_{sim} is defined by $P_{sim} \triangleq 0.5\pi R^2 \rho v^3$.

According to (18), ΔT_{rot} can be calculated by

$$\Delta T_{rot} \approx \frac{\partial T_{rot}}{\partial \omega_r}\Delta\omega_r + \frac{\partial T_{rot}}{\partial \beta}\Delta\beta + \frac{\partial T_{rot}}{\partial v}\Delta v \tag{19}$$

$$\frac{\partial T_{rot}}{\partial \omega_r} = -\frac{P_{sim} C_p}{\omega_{r0}^2} + \frac{P_{sim}}{\omega_{r0}} \cdot \frac{\partial C_p}{\partial \omega_r} \tag{20}$$

$$\frac{\partial T_{rot}}{\partial \beta} = \frac{\partial T_{rot}}{\partial \theta}\frac{\partial \theta}{\partial \beta} = \frac{\partial T_{rot}}{\partial \theta} \cdot \frac{1}{k_{a1} + 2k_{a2}\theta_0} \tag{21}$$

$$\frac{\partial T_{rot}}{\partial v} = \frac{0.5\rho\pi R^2 \cdot 3v_0^2 \cdot C_{p0}}{\omega_{r0}} \tag{22}$$

where C_p is described in a lookup table derived from the inputs λ and θ, as is shown in Table 2. Where n and m are the corresponding rows and columns, respectively.

Table 2. Lookup table of C_p (λ, θ).

θ \ λ	λ_{min}	$\lambda_{min} + \Delta\lambda$	⋯	λ_{max}
θ_{min}	0.0005	0.001	…	−0.8478
$\theta_{min} + \Delta\theta$	0.0005	0.001	…	−0.8637
…	…	…	…	…
θ_{max}	−0.0012	−0.0036	…	−207.6793

The generator torque reference T_{g_ref} is filtered by a low-pass filter and the generator torque T_g is derived by,

$$T_g = \frac{1}{1 + s \cdot \tau_g} T_{g\_ref} \tag{23}$$

where τ_g is the time constant of the filter of T_{g_ref}. T_{g_ref} is calculated by

$$T_{g-ref} = \frac{P_{ref}^{wt}}{\omega_g} \tag{24}$$

According to (23) and (24), ΔT_g and ΔT_{g_ref} can be calculated by

$$\Delta T_g \approx \frac{1}{\tau_g}\left(\frac{\partial T_g}{\partial t}\Delta t + \frac{\partial T_g}{\partial T_{g\_ref}}\Delta T_{g\_ref}\right) = -\frac{1}{\tau_g}\cdot T_{g0}\cdot \Delta t + \frac{T_{g0}}{T_{g\_ref0}}\cdot \Delta T_{g\_ref} \tag{25}$$

$$\Delta T_{g\_ref} \approx -\frac{P_{ref0}^{wt}}{\omega_{g0}^2}\Delta\omega_g + \frac{1}{\omega_{g0}}\Delta P_{ref}^{wt} \tag{26}$$

where Δt is the control cycle.

According to (14)–(17), the continuous state space model for WT is formulated as

$$\dot{\boldsymbol{x}} \approx \boldsymbol{A}\boldsymbol{x} + \boldsymbol{J}\Delta P_{ref}^{wt} + \boldsymbol{E} \tag{27}$$

where $x \approx \left[\Delta\omega_g, \Delta\beta, \Delta\omega_f, \Delta\omega_r\right]$, and the state space matrices are

$$\boldsymbol{A} = \begin{bmatrix} \frac{1}{J_g}\left(1-\frac{J_r}{J_t}\right)\frac{T_{g0}}{\omega_{g0}} & \frac{1}{J_g}\left(1-\frac{J_r}{J_t}\right)\frac{1}{\eta_g}\frac{\partial T_{rot}}{\partial\beta} & 0 & \frac{1}{J_g}\left(1-\frac{J_r}{J_t}\right)\frac{1}{\eta_g}\frac{\partial T_{rot}}{\partial\omega_r} \\ \frac{k_p}{\tau_f} & 0 & -\frac{k_p}{\tau_f}+k_i & 0 \\ \frac{1}{\tau_f} & 0 & -\frac{1}{\tau_f} & 0 \\ \frac{\eta_g}{J_t}\frac{T_{g0}}{\omega_{g0}} & \frac{1}{J_t}\frac{\partial T_{rot}}{\partial\beta} & 0 & \frac{1}{J_t}\frac{\partial T_{rot}}{\partial\omega_r} \end{bmatrix}$$

$$\boldsymbol{J} = \begin{bmatrix} \frac{1}{J_g}\left(1-\frac{J_r}{J_t}\right)\frac{T_{g0}}{\omega_{g0}} \\ 0 \\ 0 \\ -\frac{\eta_g T_{g0}}{J_t P_{ref0}^{wt}} \end{bmatrix}$$

$$\boldsymbol{E} = \begin{bmatrix} \frac{1}{J_g}\left(1-\frac{J_r}{J_t}\right)\left(\frac{T_{g0}}{\tau_g}\cdot\Delta t + \frac{T_{rot0}}{\eta_g} - T_{g0}\right) \\ K_i(\omega_{f0}-\omega_{g-rated}) \\ 0 \\ \frac{1}{J_t}\frac{\partial T_{rot}}{\partial v}\Delta v + \frac{\eta_g}{J_t}\frac{T_{g0}}{\tau_g}\cdot\Delta t + \frac{1}{J_t}\left(T_{rot0}-\eta_g T_{g0}\right) \end{bmatrix}$$

These matrices change every other dispatch cycle. Then, the continuous state space model is discretized with the sampling period t_s, which is

$$\boldsymbol{x}(k+1) \approx \boldsymbol{G}\boldsymbol{x}(k) + \boldsymbol{H}\Delta P_{ref}^{wt} + \boldsymbol{M} \tag{28}$$

with

$$\boldsymbol{G} = e^{\boldsymbol{A}t_s}$$

$$\boldsymbol{H} = \int_0^{t_s} e^{At_s} J dt$$

$$\boldsymbol{M} = \int_0^{t_s} e^{At_s} E dt$$

Substituting (6) and (11), the shaft torque T_s can be calculated by

$$T_s = T_{rot} - J_r\dot{\omega}_r - B(\omega_r - \frac{\omega_g}{\eta_g}) = (1 - \frac{J_r}{J_t})T_{rot} + \frac{\eta_g J_r}{J_t}T_g - B(\omega_r - \frac{\omega_g}{\eta_g}) \tag{29}$$

Accordingly,

$$\Delta T_s = (1 - \frac{J_r}{J_t})\Delta T_{rot} + \frac{\eta_g J_r}{J_t}\Delta T_g - B(\Delta\omega_r - \frac{\Delta\omega_g}{\eta_g}) \tag{30}$$

Based on (19) and (25), (30) can be transformed into

$$\Delta T_s(k) \approx \boldsymbol{C}^{Ts}\boldsymbol{x}(k) + \boldsymbol{D}^{Ts}\Delta P_{ref}^{wt} + \boldsymbol{F}^{Ts} \tag{31}$$

with

$$\boldsymbol{C}^{Ts} = \begin{bmatrix} \frac{B}{\eta_g} - \frac{\eta_g J_r}{J_t}\frac{T_{g0}}{\omega_{g0}} & (1 - \frac{J_r}{J_t})\frac{\partial T_{rot}}{\partial\beta} & 0 & (1 - \frac{J_r}{J_t})\frac{\partial T_{rot}}{\partial\omega_r} - B \end{bmatrix}$$

$$\boldsymbol{D}^{Ts} = \frac{\eta_g J_r}{J_t}\frac{T_{g0}}{P_{ref0}^{wt}}$$

$$\boldsymbol{F}^{Ts} = (1 - \frac{J_r}{J_t})\frac{\partial M_{rot}}{\partial v_{rot}}\Delta v_{rot} - \frac{\eta_g J_r}{J_t}\frac{T_{g0}}{\tau_g}\Delta t$$

Based on (28) and (31)

$$\Delta T_s(k+1) = \boldsymbol{C}^{Ts}\boldsymbol{x}(k+1) + \boldsymbol{D}^{Ts}\Delta P_{ref}^{wt} + \boldsymbol{F}^{Ts} \tag{32}$$

Hence

$$\Delta T_s(k+1) = (\boldsymbol{C}^{Ts}\boldsymbol{H} + \boldsymbol{D}^{Ts})\Delta P_{ref}^{wt} + \boldsymbol{C}^{Ts}\boldsymbol{G}\boldsymbol{x}(k) + \boldsymbol{C}^{Ts}\boldsymbol{M} + \boldsymbol{F}^{Ts} \tag{33}$$

In order to simplify the expressions, $a_{T_s}^i$ and $b_{T_s}^i$ are defined by

$$a_{T_s}^i \triangleq \boldsymbol{C}^{Ts}\boldsymbol{H} + \boldsymbol{D}^{Ts} \tag{34}$$

$$b_{T_s}^i \triangleq \boldsymbol{C}^{Ts}\boldsymbol{G}\boldsymbol{x}(k) + \boldsymbol{C}^{Ts}\boldsymbol{M} + \boldsymbol{F}^{Ts} \tag{35}$$

Therefore, the fatigue load sensitivity of the drive train can be expressed as

$$\frac{\partial T_s^i}{\partial P_{demand}^{WTi}} \approx \frac{\Delta T_s^i}{\Delta P_{ref}^{wti}} = a_{T_s}^i + \frac{b_{T_s}^i}{\Delta P_{ref}^{wti}} \tag{36}$$

According to [43], The tower dynamics is not included in the simplified WT model. According to, it is assumed the tower base overturning moment M_t can be approximately derived by

$$M_T \approx H{\cdot}F_T \tag{37}$$

where H is the tower height. F_t is thrust force.

The thrust force F_t is calculated by

$$F_T = 0.5\pi R^2\rho v^2 C_t(\lambda,\theta) \tag{38}$$

where C_t is the thrust coefficient.

Accordingly

$$\Delta F_t = \frac{\partial F_t}{\partial\omega_g}\Delta\omega_g + \frac{\partial F_t}{\partial\beta}\Delta\beta + \frac{\partial F_t}{\partial v}\Delta v \tag{39}$$

$$\frac{\partial F_{\mathrm{t}}}{\partial v} = 0.5\rho\pi R^2 \cdot 2v_0 \cdot C_{\mathrm{t0}} \tag{40}$$

Similar to (31),

$$\Delta F_{\mathrm{t}}(k) \approx \boldsymbol{C}^{Ft}\boldsymbol{x}(k) + \boldsymbol{F}^{Ft} \tag{41}$$

with

$$\boldsymbol{C}^{Ft} = \begin{bmatrix} 0 & \frac{\partial F_{\mathrm{t}}}{\partial \beta} & 0 & \frac{\partial F_{\mathrm{t}}}{\partial \omega_{\mathrm{g}}} \end{bmatrix}$$

$$\boldsymbol{F}^{Ft} = \frac{\partial F_{\mathrm{t}}}{\partial v}\Delta v$$

Based on (28) and (41)

$$\Delta F_{\mathrm{t}}(k+1) \approx \boldsymbol{C}^{Ft}\boldsymbol{x}(k+1) + \boldsymbol{F}^{Ft} \tag{42}$$

Hence

$$\Delta F_{\mathrm{t}}(k+1) = \boldsymbol{C}^{Ft}\boldsymbol{H}\Delta P_{\mathrm{ref}}^{\mathrm{wt}} + \boldsymbol{C}^{Ft}\boldsymbol{G}\boldsymbol{x}(k) + \boldsymbol{C}^{Ft}\boldsymbol{M} + \boldsymbol{F}^{Ft} \tag{43}$$

Similar to (34) and (35),

$$a_{F_{\mathrm{t}}}^{i} = \boldsymbol{C}^{Ft}\boldsymbol{H} \tag{44}$$

$$b_{F_{\mathrm{t}}}^{i} = \boldsymbol{C}^{Ft}\boldsymbol{G}\boldsymbol{x}(k) + \boldsymbol{C}^{Ft}\boldsymbol{M} + \boldsymbol{F}^{Ft} \tag{45}$$

Therefore, the fatigue load sensitivity of the tower structure can be expressed as

$$\frac{\partial F_{\mathrm{T}}^{i}}{\partial P_{\mathrm{demand}}^{WTi}} \approx \frac{\Delta F_{\mathrm{T}}^{i}}{\Delta P_{\mathrm{ref}}^{wti}} = a_{F_{\mathrm{T}}}^{i} + \frac{b_{F_{\mathrm{T}}}^{i}}{\Delta P_{\mathrm{ref}}^{wti}} \tag{46}$$

The fatigue load sensitivities considered in the paper are dynamic loads causing structural damage. The equation shown in (33) and (42) are not equations for calculating a fatigue load, but equations for calculating the change in the shaft torque ΔM_{s} and the tower bending moment ΔM_{t} associated with the fatigue load. The parameters in the equation are changing at different times. By reducing ΔM_{s} and ΔM_{t}, the corresponding fatigue load can be reduced. The calculations are carried out by this law of effect. Reductions on the changes of the moments ΔM_{s} and ΔM_{t} are highly corelated to reductions in the damage equivalent fatigue load [44]. ΔM_{s} and ΔM_{t} are related to changes in power reference. ΔM_{s} and ΔM_{t} can be reduced by properly distributing the active power. ΔM_{s} and ΔM_{t} are reduced for each sampling period, so the fatigue loads are reduced.

4.2. Cost Function and Constraints

In Figure 1, every individual WT is equipped with an exclusive control system that can follow the power references provided by the frequency adjustment controller.

The controller minimizes the variation of shaft torque T_{s} and thrust force F_{t} to reduce the fatigue load. Accordingly, the cost function is expressed as

$$\min \sum_{i=1}^{n} \left[\left(\frac{\partial F_{\mathrm{T}}^{i}}{\partial P_{demand}^{WTi}} \right)^2 + \xi \cdot \left(\frac{\partial M_{\mathrm{s}}^{i}}{\partial P_{demand}^{WTi}} \right)^2 \right] \tag{47}$$

For the convenience of calculation, the equivalent calculation formula is expressed as

$$\min \sum_{i=1}^{n} \left[\left(a_{T_{\mathrm{s}}}^{i} \Delta P_{ref}^{i} + b_{T_{\mathrm{s}}}^{i} \right)^2 + \xi \cdot \left(a_{F_{\mathrm{t}}}^{i} \Delta P_{ref}^{i} + b_{F_{\mathrm{t}}}^{i} \right)^2 \right] \tag{48}$$

where ξ is the weight coefficient.

$$\Delta P_{\mathrm{ref}}^{i} = P_{\mathrm{ref}}^{i} - P_{\mathrm{k}}^{i} \tag{49}$$

The constraints are expressed by

$$\sum_{i=1}^{n} P_{ref}^{i} = P_{\text{demand}}^{\text{WF}} \tag{50}$$

$$10\% P_{\text{available}}^{WTi} \le P_{\text{ref}}^{WTi} \le P_{\text{available}}^{WTi} \tag{51}$$

where $P_{\text{demand}}^{\text{WF}}$ is the demanded power of WF; $P_{\text{available}}^{WTi}$ is the maximum available power of WT-*i*, it can be estimated by

$$P_{\text{available}}^{WTi} = \min(P_{\text{rated}}^{i}, 0.5\pi R_i^2 v_{\text{nac}}^3 C_{\text{p}}^{i}) \tag{52}$$

where P_{rated}^{i} is the rated power of WT; v_{nac} is the nacelle wind speed of WT. The corresponding data of C_{p} and C_{t} for this study can be accessed in the wind turbine model of SimWindFarm. The plot of $C_{\text{p}}(\lambda, \theta)$ and $C_{\text{t}}(\lambda, \theta)$ based on the lookup table is shown in Appendix A.

The presented problems can be expressed as standard quadratic programming (QP) issues [45,46]. It can be effectively solved by a commercial solver. This optimization problem can be solved by different optimization methods. Group intelligent algorithms such as particle swarm optimization (PSO) and genetic algorithm (GA) have good search performance for solving complex problems, but the calculation time is long and is not suitable for real-time online optimization [47–50]. The programming algorithm has a good ability to search for non-complex solving problems, and the calculation time is short, which is suitable for online optimization. The model proposed in this paper belongs to the non-complex online solution model.

Then, the matrix $\boldsymbol{H}$ and the matrix $\boldsymbol{f}$ of QP can be expressed as

$$\boldsymbol{H} = diag\left\{2(a_{T_{\text{s}}}^{1})^2 + 2\xi(a_{F_{\text{t}}}^{1})^2, 2(a_{T_{\text{s}}}^{2})^2 + 2\xi(a_{F_{\text{t}}}^{2})^2, \cdots, 2(a_{T_{\text{s}}}^{n})^2 + 2\xi(a_{F_{\text{t}}}^{n})^2\right\} \tag{53}$$

$$\boldsymbol{f} = \begin{bmatrix} 2a_{T_{\text{s}}}^{1}(b_{T_{\text{s}}}^{1} - a_{T_{\text{s}}}^{1}P_0^1) + 2\xi a_{F_{\text{t}}}^{1}(b_{F_{\text{t}}}^{1} - a_{F_{\text{t}}}^{1}P_0^1) \\ 2a_{T_{\text{s}}}^{2}(b_{T_{\text{s}}}^{2} - a_{T_{\text{s}}}^{2}P_0^2) + 2\xi a_{F_{\text{t}}}^{2}(b_{F_{\text{t}}}^{2} - a_{F_{\text{t}}}^{2}P_0^2) \\ \vdots \\ 2a_{T_{\text{s}}}^{n}(b_{T_{\text{s}}}^{n} - a_{T_{\text{s}}}^{n}P_0^n) + 2\xi a_{F_{\text{t}}}^{n}(b_{F_{\text{t}}}^{n} - a_{F_{\text{t}}}^{n}P_0^n) \end{bmatrix} \tag{54}$$

If the available power of WF does not meet the demand, the following procedure is available.

$$if: \sum_{i=1}^{n} P_{available}^{WTi} \le P_{\text{demand}},\ P_{\text{ref}}^{i} = P_{\text{available}}^{WTi} \tag{55}$$

5. Case Study

5.1. System Setup

The WF control architecture illustrated in Figure 1 is used to test the performance of control. Figure 1 shows the typical configuration of a WF, which consists of 10, 5 MW WTs. The simulation model is based on SimWindFarm [40] developed in the EU-FP7 project by AEOLUS. The SimWindFarm model allows the real time simulation of flows in the wind field and includes the main aerodynamic effects of the wind farm in MATLAB/Simulink. It consists of four elementary components: wind turbine dynamics, wind field interactions and dynamics, wind farm controller, and electrical network operator. It can represent the main dynamics of a wind farm. The model toolbox includes a wind field generator where mean wind speed, turbulence intensity, and grid resolution can be specified. Furthermore, a number of post-processing tools are included for performance, such as a rain-flow counting algorithm and wake animation. Simulations are conducted for WF over 200 s of run time.

In the test system, the frequency adjustment controller of WF sends instructions every 0.5 s. 0.5 s is to match the wind farm dispatch algorithm and faster to achieve frequency regulation. The parameters of frequency adjustment controller are shown in Table 3. The PRD optimization (OPT) controllers send instructions every 0.5 s. The detailed WT parameters are listed in Table 4. The typical turbulent winds with different intensities generated by the Aeolus toolbox with same average wind speed of 12 m/s are shown in Figure 5.

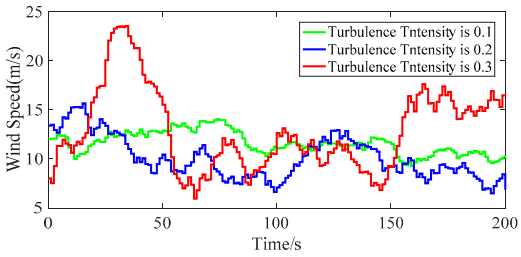

Figure 5. Typical turbulent winds with different intensities generated by the Aeolus toolbox with same average wind speed of 12 m/s.

Table 3. Parameters of Fuzzy-PID controller.

Parameter	Value
f_N	50 Hz
a_P	1×10^8
b_P	3×10^8
a_I	5×10^6
b_I	5×10^7
a_D	5×10^7
b_D	2×10^8

Table 4. Parameters of WT.

Parameter	Value
Rotor inertia: J_r	3.54×10^7 (kg·m^2)
Generator inertia: J_g	5.34×10^2 (kg·m^2)
Gear box ratio: η_g	97
Filter time constant of ω_g: τ_f	10
Proportional gain: k_p	0.2143
Integral gain: k_i	0.0918
Gain coefficient: k_{a1}	2.1323
Gain coefficient: k_{a2}	1
Generator rated speed: $\omega_{g\text{-rated}}$	122.91 (rad/s)
Main shaft viscous friction coefficient: B	6.22×10^6 (Nm·s/rad)
Sir density: ρ	1.22 (kg/m^3)
Length of the blade: R	63 (m)
Filter time constant of T_{g_ref}: τ_g	0.1

Through post-processing, the fatigue cycles based on the rainflow counting method are derived to evaluate the performance of the proposed method. Furthermore, the damage equivalent load (DEL) is based on the Miner's rule and depends on the material properties specified by the slope of the S–N curve for quantizing the load minimization. In this study, the relevant calculations are performed by MCrunch developed by NREL [51].

5.2. Wind Farm Controller Performance

5.2.1. Performance for the Improved Model of Fatigue Load Sensitivity

In the simple WT model, the drive train can be considered to be rigid if the fatigue load is ignored. However, the drive train is a flexible system. A comparison of measured ω_r and $\frac{\omega_g}{\eta_g}$ is shown in Figure 6. As shown in Figure 6, $\omega_r \neq \frac{\omega_g}{\eta_g}$. So $\Delta\omega_g(k)$ and $\Delta\omega_r(k)$ are calculated separately in the improved models, and the calculation formula of $\omega_g = \eta_g\omega_r$ is not used.

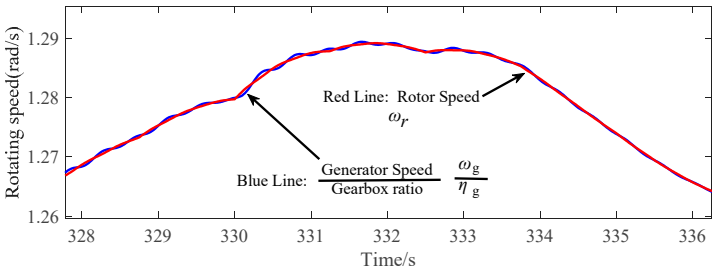

Figure 6. Wind speed, and the measured ω_r and $\frac{\omega_g}{\eta_g}$ in a flexible system.

The wind speed of the WF is 12 m/s with 0.1 turbulence intensity. The values of $\Delta\omega_g(k+1)$ and $\Delta\omega_r(k+1)$ obtained by calculating WT1 are shown in Figures 7 and 8. Note that $x(k+1)$ is obtained by discretizing $x(k)$. Figures 7, 8, 9 and 10b are enlarged image of the inside of the dashed box in Figures 7, 8, 9 and 10a, which will not be described in detail in the following paper.

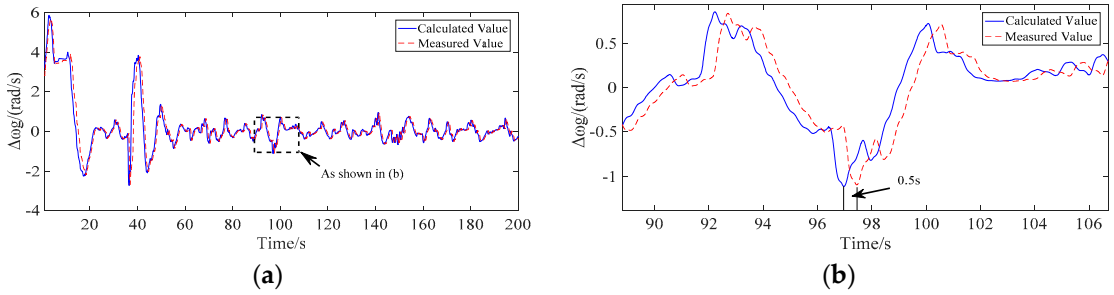

Figure 7. Calculated and measured values of $\Delta\omega_g$. (**a**) Calculated and measured values of $\Delta\omega_g$ from 0 to 200 seconds; (**b**) Calculated and measured values of $\Delta\omega_g$ from 89 to 106 seconds.

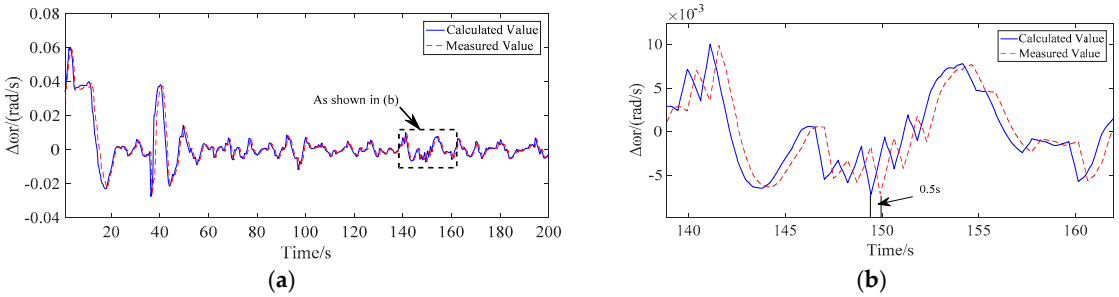

Figure 8. Calculated and measured values of $\Delta\omega_r$. (**a**) Calculated and measured values of $\Delta\omega_r$ from 0 to 200 seconds; (**b**) Calculated and measured values of $\Delta\omega_r$ from 139 to 162 seconds.

As is shown in Figures 7b and 8b, The values of $\Delta\omega_g$ and $\Delta\omega_r$ after 0.5 s can be accurately calculated using the improved model. A better basis for optimizing results is provided by this precise calculation.

The effect of changes in wind speed is considered when calculating ΔT_{rot}. Comparison of the case of adding $\frac{\partial T_{rot}}{\partial v}\Delta v$ and not adding is shown in Figure 9.

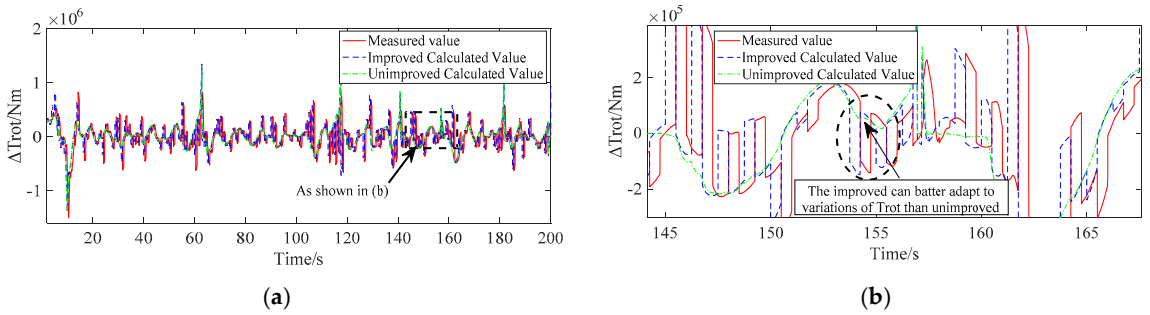

(**a**) (**b**)

Figure 9. Calculated and measured values of ΔT_{rot}. (**a**) Calculated and measured values of ΔT_{rot} from 0 to 200 seconds; (**b**) Calculated and measured values of ΔT_{rot} from 144 to 167 seconds.

The model is simulated based on SimWindFarm. Since the control time is 0.5 s, sampling is performed every 0.5 s. Because T_{rot} is cube of v, even small changes of v can have a big impact on ΔT_{rot}. As is shown in Figure 9b, in the vicinity of 154 s, there is a big step in the measured value, which is caused by the change in wind speed. Mutations in ΔT_{rot} caused by sudden changes in wind speed can still be accurately calculated by the improved model. However, the original models that did not consider $\frac{\partial T_{\text{rot}}}{\partial v}\Delta v$ cannot adapt to this mutation. The value of ΔT_{rot} after 0.5 s is accurately calculated.

After a detailed improvement, the ΔF_{t} calculation is more accurate. The comparison between the improved value and the measured value is shown in Figure 10.

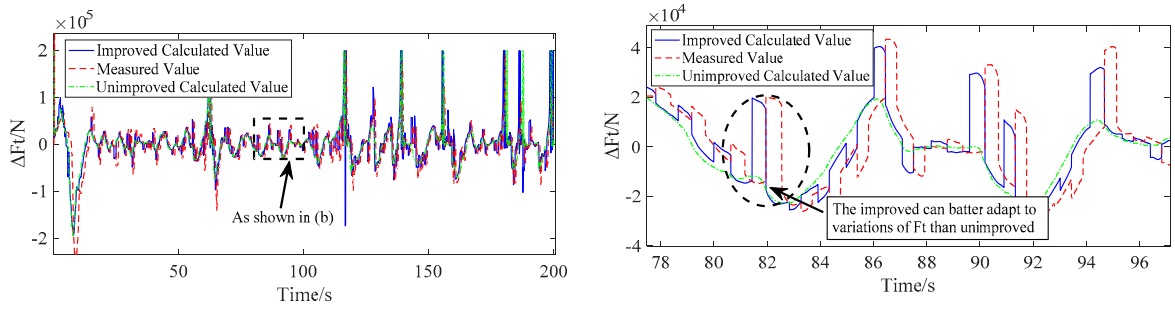

(**a**) (**b**)

Figure 10. Calculated and measured values of ΔF_{t}. (**a**) Calculated and measured values of ΔF_{t} from 0 to 200 seconds; (**b**) Calculated and measured values of ΔF_{t} from 78 to 97 seconds.

As is shown in Figure 10b. In the vicinity of 82 s, there is a big step in the measured value, which is caused by the change in wind speed. The improved model can better adapt to the ΔF_{t} mutation like ΔT_{rot}. This improvement makes the calculation of the optimization target more accurate and the optimization effect is better. The re-derived fatigue load sensitivity equations can improve the calculation accuracy very well.

5.2.2. Performance for Different Turbulence Intensity

The normal PRD controller uses a proportional distribution method (NORM). The reference power is assigned to the WT in the available power ratio. As is calculated by

$$P_{\text{ref}}^{WTi} = \frac{P_{\text{available}}^{WTi}}{\sum_{i=1}^{n} P_{available}^{WTi}} P_{\text{demand}}^{\text{WF}} \tag{56}$$

In order to test the efficacy of the improved model, the operation of wind farm under different turbulence intensity were studied and the FAC is not used. The average wind speed of the test wind is 12 m/s, and the turbulence intensity is 0.1, 0.2, and 0.3 respectively. The results of OPT and NORM are

compared under different turbulence intensities. The tower bending moment was mainly considered in this paper, so the weight coefficient ξ to 3000 is selected.

Scenario 1: The turbulence intensity is 0.1. The wind farm reference power $P_{\text{demand}}^{\text{WF}}$ is 35 MW under this scenario. The calculated DELs of T_{s} and M_{t} for all WTs are listed in Table 5. As shown in Table 5, some of the WTs have more growth in DELs for T_{s}, but this growth will be offset as the simulation time increases. The total DELs of wind farms using OPT is still lower than NORM. From the whole WF point of view, the reductions of the total DEL for T_{s} is 2.21%.

Table 5. DELs of T_{s} and F_{t} for Scenario 1.

No.	DELs for WTs (T_{s}/MNm)			DELs for WTs (M_{t}/MNm)		
	NORM	OPT	Percentage	NORM	OPT	Percentage
1	1.94	2.06	6.13%	50.48	44.96	−10.93%
2	1.94	1.76	−9.38%	57.48	57.92	0.77%
3	1.82	1.77	−2.26%	62.68	60.90	−2.83%
4	1.82	1.70	−6.73%	54.19	47.86	−11.68%
5	1.85	2.28	23.39%	42.83	40.86	−4.59%
6	1.86	1.66	−11.04%	59.97	58.95	−1.71%
7	1.74	1.55	−10.86%	65.75	64.67	−1.64%
8	1.83	1.45	−20.89%	48.69	40.87	−16.05%
9	1.87	2.08	11.01%	42.00	38.29	−8.83%
10	1.80	1.76	−2.48%	58.64	58.56	−0.15%
summary	18.47	18.07	−2.21%	542.76	513.90	−5.32%

Compared with the NORM, most DELs of M_{t} except for NO.2 are reduced. The reduction values are from 0.15% to 16.05%. From the whole WF point of view, the total DEL of Mt is reduced by 5.32%.

Scenario 2: The turbulence intensity is 0.2. The wind farm reference power is 20 MW under this scenario. Scenario 3: The turbulence intensity is 0.3. The wind farm reference power is 15 MW under this scenario. The calculated DELs of T_{s} and M_{t} for the sum of all WTs are listed in Table 6.

Table 6. DELs of T_{s} and F_{t} for Scenario 2 and 3.

Turbulence Intensity	DELs for WTs (T_{s}/MNm)			DELs for WTs (M_{t}/MNm)		
	NORM	OPT	Percentage	NORM	OPT	Percentage
0.2	15.78	14.97	−5.13%	616.40	577.77	−6.28%
0.3	14.63	14.27	−2.46%	646.93	611.33	−5.50%

As shown in Table 6, the DELs of both T_{s} and M_{t} with the OPT are reduced compared with NORM.

When the turbulence intensity is 0.2, a more detailed cumulative rainflow cycle is shown in Figure 11. A representative WT (WT09) is used as an example. Compared with the NORM, less cycles are found for OPT, which implies less fatigue loads experienced by the WT.

When the turbulence intensity is 0.3, a more detailed cumulative rainflow cycle is shown in Figure 12. A representative WT02 is used as an example. Compared with the NORM, less cycles are found for OPT, which implies less fatigue loads experienced by the WT.

Fatigue load optimization results with three different turbulence intensities were obtained. It can be seen from the results that the improved model can optimize the fatigue load well under different turbulence intensities.

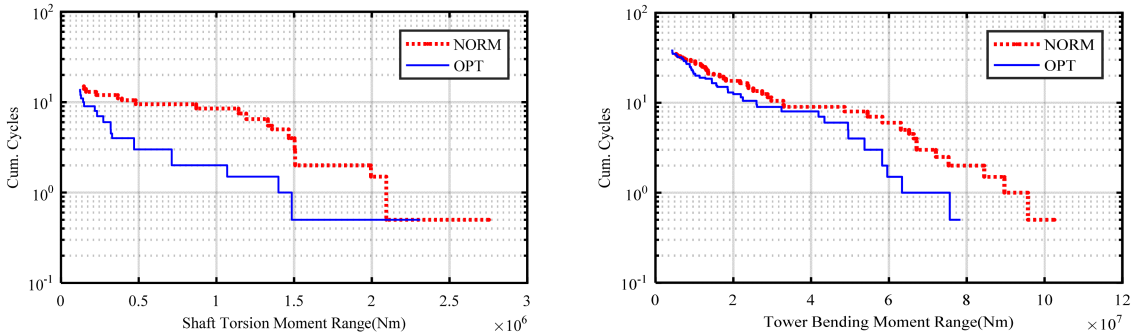

(**a**) (**b**)

Figure 11. Cumulative rainflow cycle of T_s and M_t of WT09 for 0.2 turbulence intensity. (**a**) Cumulative rainflow cycle of Shaft Torsion Moment for 0.2 turbulence intensity; (**b**) Cumulative rainflow cycle of Tower Bending Moment for 0.2 turbulence intensity.

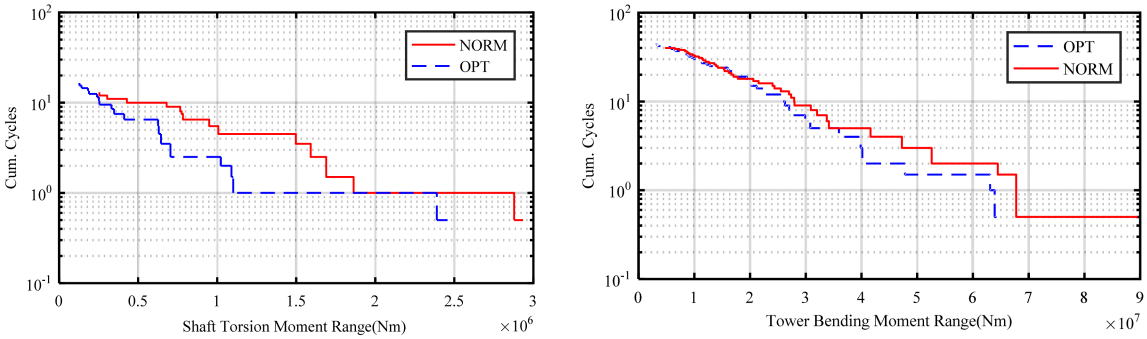

(**a**) (**b**)

Figure 12. Cumulative rainflow cycle of T_s and M_t of WT02 for 0.3 turbulence intensity. (**a**) Cumulative rainflow cycle of Shaft Torsion Moment of WT02 for 0.3 turbulence intensity; (**b**) Cumulative rainflow cycle of Tower Bending Moment of WT02 for 0.3 turbulence intensity.

5.3. Overall Performance

5.3.1. WF Controller Performance

In order to prove the performance of the frequency control of the developed solution, the wind farm is assumed to be able to get enough power from the wind. When the WF is operating in the frequency regulation mode, the measured grid frequency is used as a feedback signal to establish real-time active power control. The baseline model for electrical network operator in SimWindFarm can function in different power command modes such as: absolute, delta, and frequency regulation modes. Basically, baseline control scheme in frequency regulation mode can maintain the necessary balance between power generation and loads. The demand power of the baseline control is calculated by

$$P_{\text{demand}}^{\text{WF}} = \begin{cases} 0.5 \times P_{\text{up}} & -t_{\text{d}} \le f_{\text{error}} \le t_{\text{d}} \\ 0.5 \times (P_{\text{up}} - P_{\text{down}}) & t_{\text{c}} \le f_{\text{error}} \\ 0.5 \times (P_{\text{up}} + P_{\text{down}}) & f_{\text{error}} \le -t_{\text{c}} \\ 0.5 \times P_{\text{up}} - 0.5 \times P_{\text{down}}(\frac{f_{\text{error}} - t_{\text{d}}}{t_{\text{c}} - t_{\text{d}}}) & t_{\text{d}} < f_{\text{error}} < t_{\text{c}} \\ 0.5 \times P_{\text{up}} - 0.5 \times P_{\text{down}}(\frac{f_{\text{error}} + t_{\text{d}}}{t_{\text{c}} - t_{\text{d}}}) & -t_{\text{c}} < f_{\text{error}} < -t_{\text{d}} \end{cases} \quad (57)$$

where t_{d} and t_{c} are two constants ($t_{\text{c}} > t_{\text{d}}$) of dead bands and control bands, defined by $t_{\text{d}} = 0.002$ and $t_{\text{c}} = 0.02$ which can enable the baseline control to function optimally. Moreover, P_{up} and P_{down} are defined by

$$P_{\text{up}} = P_{\text{max}} + P_{\text{min}} \quad (58)$$

$$P_{\text{down}} = P_{\max} + P_{\min} \tag{59}$$

where $P_{\min}$ and $P_{\max}$ are the prescribed minimum and maximum limits for the total power of WF.

In order to verify the performance of the control method, different functions of the grid load are defined and used for WF testing. Baseline control is compared to Fuzzy-PID. NORM dispatch method is compared to OPT method. The initial frequency is assumed to be 50 Hz. The test wind is 12 m/s with 0.3 turbulence intensity. Figures 13a and 14a show the performance of the active power control method for the WF in response to the different loads considered, respectively. Figures 13b and 14b show the grid frequency responses with respect to the different loads, respectively. The power and frequency responses of Fuzzy-PID and baseline control are compared in Figures 13 and 14, respectively. The power curve of the wind farm output is the same whether the WF dispatch method uses NORM or OPT.

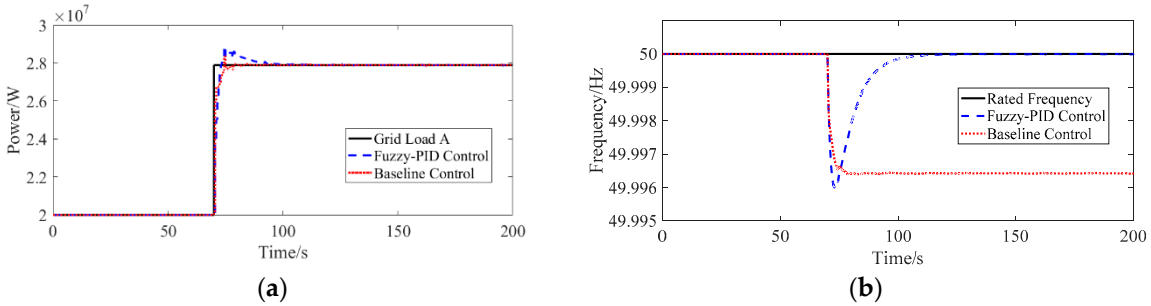

Figure 13. Total active power and grid frequency response during grid load A. (**a**) Active power response during grid load A; (**b**) Grid frequency response during grid load A.

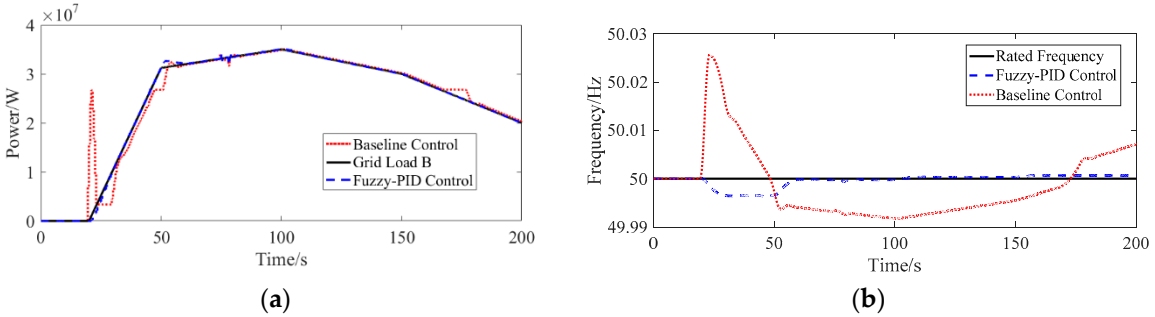

Figure 14. Total active power and grid frequency response during grid load B. (**a**) Active power response during grid load B; (**b**) Grid frequency response during grid load B.

As shown in Figure 13a, the grid load A is a step variable. As is shown in Figure 13b, the baseline control cannot achieve a frequency of 50 Hz, and there is still an error of 0.004 Hz as the control time increases. The frequency error of the Fuzzy-PID control method is smaller than that of the baseline control. As the control time increases, the frequency gradually approaches 50 Hz and the error disappears. The Fuzzy-PID control method can quickly track the frequency so that the error is approximately zero at the 100 s. Therefore, the Fuzzy-PID method has better control effects than the baseline control.

As is shown in Figure 14a, grid load B is the varying load. Baseline control failed to track the grid load during the initial phase of 20–50 s, which also caused a relatively large frequency fluctuation of 20–50 s as shown in Figure 14b. Fuzzy-PID control can track grid load very well by compared to baseline control. As is shown in Figure 14b, Fuzzy-PID can track the frequency very well, and the frequency error of Fuzzy-PID is smaller. As are shown in Figures 13 and 14, less power fluctuations make power tracking better.

To check the tracking accuracy of APC methods, the normalized root-mean-squared error (NRMSE) is defined as

$$NRMSE = \frac{\sqrt{\frac{1}{N}\sum_{i=1}^{N}(P_{\mathrm{L}} - P_{out})^2}}{\overline{P_{\mathrm{out}}}} \tag{60}$$

To illustrate the ability of Fuzzy-PID methods in the regulation of the grid frequency, Table 7 quantitatively compares the obtained grid frequency responses in terms of standard deviation (SD) and NRMSE of power responses.

Table 7. Quantitative comparison of Fuzzy-PID methods in terms of accuracy of response for active power and frequency.

Control Method	NRMSE for Power Responses		SD for grid Frequency Responses	
	Grid Load A	Grid Load B	Grid Load A	Grid Load B
Baseline Control	0.017545	0.104380	0.002845	0.007423
Fuzzy-PID	0.021409	0.012052	0.000764	0.001345

For a step grid load like A, compared to baseline control, NRMSE for power responses increased by 22.02%, and SD for grid frequency responses is reduced by 88.45%. For a varying grid load like B, compared to baseline control, NRMSE for power responses is reduced by 73.15% and SD for grid frequency responses is reduced by 81.88%.

By testing the control method of the WF with different loads, the Fuzzy-PID control has a good performance regardless of the speed or error of the tracking frequency.

5.3.2. Fatigue Loads Performance

The fatigue load results of the WTs using Baseline Control + NORM, Fuzzy-PID + NORM and Fuzzy-PID + OPT are shown in Figure 15 when load B is used to test the overall controller.

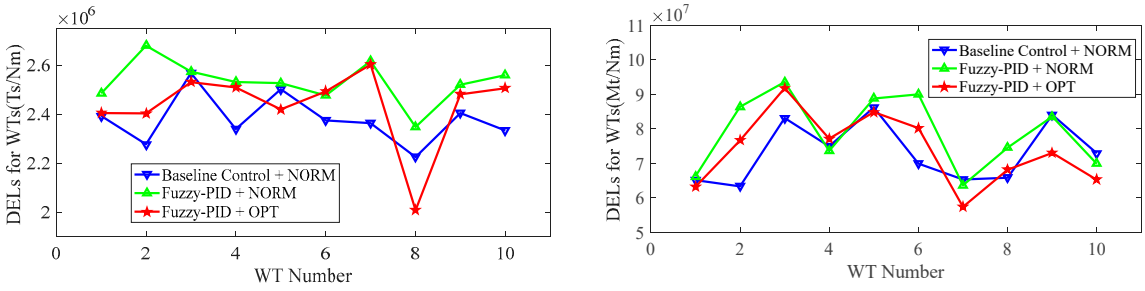

Figure 15. DELs of the WTs using Baseline Control + NORM, Fuzzy-PID + NORM and Fuzzy-PID + OPT when load B is used to test the overall controller. (**a**) DELs for Shaft Torsion Moment of the WTs; (**b**) DELs for Tower Bending Moment of the WTs.

As is shown in Figure 15, the frequency adjustment effect by the Fuzzy-PID is better, but the DELs of T_{s} is significantly larger than Baseline Control + NORM. The specific results are shown in Table 7, the fatigue load using Fuzzy-PID + NORM increased by 6.47% compared with the fatigue load using Baseline Control + NORM. The fatigue load using Fuzzy-PID + OPT still increased by 2.44% compared with Baseline Control + NORM, but decreased by 3.79% compared with Fuzzy-PID + NORM.

The fatigue load of M_{t} using Fuzzy-PID + NORM was significantly higher than that of Baseline Control + NORM, and the specific results were increased by 8.15% as shown in Table 8. The fatigue load using Fuzzy-PID + OPT is 0.32% higher than Baseline Control + NORM and 7.24% lower than Fuzzy-PID + NORM.

Table 8. Total DELs of WTs for three different controllers.

	DELs for WTs (M_t/MNm)		DELs for WTs (T_s/MNm)	
	Values	**Percentage**	**Values**	**Percentage**
Baseline Control + NORM	730.68		23.77	
Fuzzy-PID + NORM	790.23	8.15%	25.31	6.47%
Fuzzy-PID + OPT	733.01	0.32%	24.35	2.44%

The fatigue load of the WT will increase since the WF needs to frequently change the pitch angle and reference power when participating in frequency regulation. The better the frequency adjustment effect, the more frequent this change, the greater the fatigue load caused. The overall fatigue load of the WT is reduced, DELs of M_t is hardly affected especially after considering the fatigue load.

6. Conclusions

In this paper, an APC method for supporting grid frequency regulation in WFs considering fatigue load of WT is proposed. The Fuzzy-FID control is used for a frequency adjustment controller to maintain the balance between power generation and grid load. The equations of fatigue load sensitivity are re-derived. The calculation accuracy is improved by the re-derived equations. The re-derived equations are used for PRD to minimize the fatigue load for all the WTs. Case studies show that the frequency adjustment control method based on Fuzzy-PID can respond to and recover grid frequency deviations more quickly. Less power fluctuations make power tracking better. Compared to baseline control, NRMSE for power responses and SD for grid frequency of Fuzzy-PID are reduced by 81.45% and 81.88%, separately. In addition, the explicit analytical equations of fatigue load sensitivity are re-derived to improve the calculation accuracy of the fatigue loads. DELs for T_s reduced by 2.21% to 5.13%, DELs for M_t reduced by 5.32% to 7.32%. This improvement minimizes fatigue loads for wind farms under different turbulent wind and different loads. The proposed solution is suitable for real-time control of large-scale WF.

Since this study is mainly focused on the wind farm control level, some of the dynamics of WTs are ignored. Rainflow counting is applied to the time histories of thrust and torque from the simulation results, so the evaluation of fatigue load cannot be fully reflected. Quantitative conclusions are uncertain and can only represent trends in fatigue load changes. Since this study is a simulation based on SimWindFarm, the study cannot consider all practical engineering problems. Verifying this method in engineering is what we will do next.

Author Contributions: The paper was a collaborative effort among the authors. Y.W. carried out relevant theoretical research, performed the simulation, analyzed the data, and wrote the paper. Y.L. and X.W. provided critical comments. J.Z. and W.H.L. revised the paper.

Funding: This work was supported by the National Natural Science Foundation (51677121) of China and Liaoning Provincial Department of Education Serves Local Project (201734134).

Conflicts of Interest: The authors declare no conflict of interest.

Nomenclature

Symbols

K_P, K_I, K_D	Calculated by Fuzzy-PID controller
b_P, b_I, b_D	Parameters of conventional PID controller
a_P, a_I, a_D	Parameters of determined the relevant ranges of variations for b_P, b_I, and b_D
P, I, D	Calculated by Fuzzy Rules
P^{WF}_{demand}	Demanded power of wind farm
$P^{WF}_{available}$	Available power of wind farm
$P^{WTi}_{available}$	Available power of wind turbine i

P^{i}_{rated}	Rated power of wind farm
P^{WTi}_{ref}	Reference power of wind turbine i
$\frac{\partial L}{\partial P^{\text{WT}}_{\text{demand}}}$	Sensitivity of fatigue load with respect to demanded power of wind turbine
$\frac{\partial T_s}{\partial P^{\text{WT}}_{\text{demand}}}$	Sensitivity of drive train fatigue load with respect to demanded power of wind turbine
$\frac{\partial F_t}{\partial P^{\text{WT}}_{\text{demand}}}$	Sensitivity of the tower structural fatigue load with respect to demanded power of wind turbine
f_{error}	Grid frequency error
f_{meas}	Grid measured frequency
f_{N}	Normal frequency of the grid
J_{t}	Equivalent mass of the drive-train
J_{r}	Rotational inertia of the rotor
J_{g}	Rotational inertia of the generator
η_{g}	Gear box ratio
ω_{r}	Measured rotor speed
ω_{g}	Measured generator speed
$\omega_{\text{g-rated}}$	Rated generator speed
F_{t}	Thrust force
T_{rot}	Aerodynamic torque
T_{g}	Generator torque
$T_{\text{g\_ref}}$	Generator torque reference
T_{s}	Shaft torque
M_{t}	Tower basefore-aft bending moment
$T_{\text{gi}}{}^{\text{ref}}$	Generator torque of wind turbine i
ω_{f}	Generator filtered speed
τ_{f}	Time constant of the filter of ω_{g}
τ_{g}	Time constant of the filter of $T_{\text{g\_ref}}$
$\theta_{\text{i}}{}^{\text{ref}}$	Pitch angle reference of wind turbine i
θ_{ref}	Pitch angle reference of blades
k_{a}, β	Functions of θ_{ref}
$k_{\text{p}}, k_{\text{i}}$	Proportional and integral gain of θ_{ref}
$k_{\text{a1}}, k_{\text{a2}}$	Constants of k_{a}
B	Main shaft viscous friction coefficient
P_{g0}	Output power of a turbine at $t = k$
ω_{g0}	Generator speed at $t = k$
ω_{f0}	Filtered speed of the generator speed at $t = k$
θ_0	Pitch angle at $t = k$
T_{rot0}	Aerodynamic torque at $t = k$
T_{g}	Generator torque at $t = k$
R	Length of the blade
H	Tower height
ρ	Air density
v	Wind speed of hub height
C_{p}	Power coefficient
C_{t}	Thrust coefficient
λ	Tip speed ratio

Appendix A

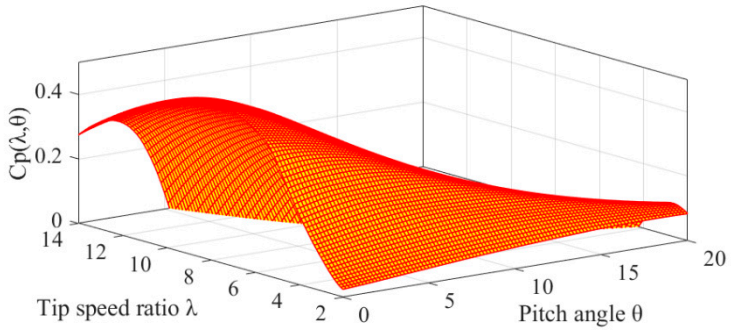

Figure A1. $C_p(\lambda, \theta)$ based on the data from SimWindFarm.

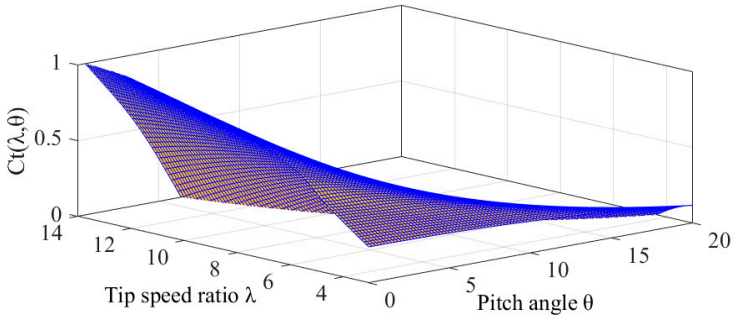

Figure A2. $C_t(\lambda, \theta)$ based on the data from SimWindFarm.

References

1. Sun, X.J.; Huang, D.G. An Explosive Growth of Wind Power in China. *Int. J. Green. Energy* **2014**, *14*, 849–860. [CrossRef]
2. Nguyen, C.-K.; Nguyen, T.-T.; Yoo, H.-J.; Kim, H.-M. Consensus-Based SOC Balancing of Battery Energy Storage Systems in Wind Farm. *Energies* **2018**, *11*, 3507. [CrossRef]
3. Bottiglione, F.; Mantriota, G.; Valle, M. Power-Split Hydrostatic Transmissions for Wind Energy Systems. *Energies* **2018**, *11*, 3369. [CrossRef]
4. Kazda, J.; Cutululis, N.A. Fast Control-Oriented Dynamic Linear Model of Wind Farm Flow and Operation. *Energies* **2018**, *11*, 3346. [CrossRef]
5. Wind Power Capacity Reaches 539 GW, 52,6 GW Added in 2017. 12 February 2018. Available online: http://wwindea.org/blog/2018/02/12/2017-statistics/ (accessed on 20 April 2019).
6. Sun, B.; Tang, Y.; Ye, L.; Chen, C.; Zhang, C.; Zhong, W. A Frequency Control Method Considering Large Scale Wind Power Cluster Integration Based on Distributed Model Predictive Control. *Energies* **2018**, *11*, 1600. [CrossRef]
7. Hou, T.T.; Lou, S.H.; Wu, Y.W. Capacity Optimization of Thermal Units Transmitted with Wind Power: A Case Study of Jiuquan Wind Power Base, China. *J. Wind. Eng. Ind. Aerod.* **2014**, *129*, 64–68. [CrossRef]
8. Dai, X.M.; Zhang, K.F.; Geng, J. Study on Variability Smoothing Benefits of Wind Farm Cluster. *Turk. J. Electr. Eng. Comput. Sci.* **2018**, *26*, 1894–1908. [CrossRef]
9. Du, W.J.; Bi, J.T.; Wang, T.; Hua, W. Impact of Grid Connection of Large-Scale Wind Farms on Power System Small-Signal Angular Stability. *CSEE JPES* **2015**, *1*, 83–89. [CrossRef]
10. Li, J.; Ye, L.; Zeng, Y.; Wang, H.F. A Scenario-Based Robust Transmission Network Expansion Planning Method for Consideration of Wind Power Uncertainties. *CSEE JPES* **2016**, *2*, 11–18. [CrossRef]
11. Liao, S.Y.; Xu, J.; Sun, Y.Z.; Bao, Y.; Tang, B.W. Wide-Area Measurement System-Based Online Calculation Method of PV Systems De-loaded Margin for Frequency Regulation in Isolated Power Systems. *IET Renew. Power. Gen.* **2018**, *12*, 335–341. [CrossRef]
12. Athari, M.H.; Wang, Z. Impacts of Wind Power Uncertainty on Grid Vulnerability to Cascading Overload Failures. *IEEE Trans. Sustain. Energy* **2018**, *9*, 128–137. [CrossRef]

13. You, R.; Barahona, B.; Chai, J.Y.; Cutululis, N.A.; Wu, X.Z. Improvement of Grid Frequency Dynamic Characteristic with Novel Wind Turbine Based on Electromagnetic Coupler. *Renew. Energy* **2017**, *113*, 813–821. [CrossRef]
14. Oest, J.; Lund, E. Topology Optimization with Finite-life Fatigue Constraints. *Struct. Multidiscip. Optim.* **2017**, *56*, 1045–1059. [CrossRef]
15. Attya, A.B.; Domínguez-García, J.L.; Bianchi, F.D.; Anaya-Lara, O. Enhancing Frequency Stability by Integrating Non-conventional Power Sources Through Multi-terminal HVDC Grid. *Int. J. Electr. Power Energy Syst.* **2018**, *95*, 128–136. [CrossRef]
16. Dijk, M.T.V.; Wingerden, J.W.V.; Ashuri, T.; Li, Y. Wind Farm Multi-Objective Wake Redirection for Optimizing Power Production and Loads. *Energy* **2017**, *121*, 561–569. [CrossRef]
17. Soleimanzadeh, M.; Wisniewski, R. Controller Design for a Wind Farm, Considering Both Power and Load Aspects. *Mechatronics* **2011**, *21*, 720–727. [CrossRef]
18. Njiri, J.G.; Beganovic, N.; Do, M.H.; Soffker, D. Consideration of Lifetime and Fatigue Load in Wind Turbine Control. *Renew. Energy* **2018**, *131*, 818–828. [CrossRef]
19. Kanev, S.K.; Savenije, F.J.; Engels, W.P. Active Wake Control: An Approach to Optimize the Lifetime Operation of Wind Farms. *Wind Energy* **2018**, *21*, 488–501. [CrossRef]
20. Madani, S.M.; Akbari, M. Analytical Evaluation of Control Strategies for Participation of Doubly Fed Induction Generator-Based Wind Farms in Power System Short-Term Frequency Regulation. *IET Renew. Power Gen.* **2014**, *8*, 324–333.
21. Leon, A.E.; Mauricio, J.M.; Gomezexposito, A.; Solsona, J.A. Hierarchical Wide-Area Control of Power Systems Including Wind Farms and Facts for Short-Term Frequency Regulation. *IEEE Trans. Power Syst.* **2012**, *27*, 2084–2092. [CrossRef]
22. Ye, H.; Pei, W.; Qi, Z. Analytical Modeling of Inertial and Droop Responses from a Wind Farm for Short-Term Frequency Regulation in Power Systems. *IEEE Trans. Power Syst.* **2015**, *31*, 3414–3423. [CrossRef]
23. Wang, Z.; Wu, W. Coordinated Control Method for DFIG-Based Wind Farm to Provide Primary Frequency Regulation Service. *IEEE Trans. Power Syst.* **2017**, *33*, 3644–3659. [CrossRef]
24. Gao, Y.; Ai, Q. Distributed Multi-agent Control for Combined AC/DC Grids With Wind Power Plant Clusters. *IET Gener. Transm. Dis.* **2018**, *12*, 670–677. [CrossRef]
25. Gao, X.D.; Meng, K.; Dong, Z.Y. Cooperation-Driven Distributed Control Method for Large-Scale Wind Farm Active Power Regulation. *IEEE Trans. Energy Convers.* **2017**, *32*, 1240–1250. [CrossRef]
26. Badihi, H.; Zhang, Y.; Hong, H. Active Power Control Design for Supporting Grid Frequency Regulation in Wind Farms. *Annu. Rev. Control.* **2015**, *40*, 70–81. [CrossRef]
27. Knudsen, T.; Bak, T.; Svenstrup, M. Survey of Wind Farm Control-Power and Fatigue Optimization. *Wind Energy* **2015**, *18*, 1333–1351. [CrossRef]
28. Zhao, H.R.; Wu, Q.W.; Guo, Q.; Sun, H.B.; Xue, Y.S. Distributed Model Predictive Control of a Wind Farm for Optimal Active Power Control—Part II: Implementation with Clustering-Based Piece-Wise Affine Wind Turbine Model. *IEEE Trans. Sustain. Energy* **2015**, *6*, 840–849. [CrossRef]
29. Zhao, H.R.; Wu, Q.W.; Guo, Q.; Sun, H.B.; Xue, Y.S. Optimal Active Power Control of a Wind Farm Equipped with Energy Storage System Based on Distributed Model Predictive Control. *IET Gener. Transm. Distrib.* **2016**, *10*, 669–677. [CrossRef]
30. Zhao, H.R.; Wu, Q.W.; Huang, S.J.; Shahidehpour, M.; Guo, Q.; Sun, H.B. Fatigue Load Sensitivity Based Optimal Active Power Dispatch for Wind Farms. *IEEE Trans. Sustain. Energy* **2017**, *8*, 1247–1259. [CrossRef]
31. Yuan, S.; Zhao, C.; Guo, L. Uncoupled PID Control of Coupled Multi-Agent Nonlinear Uncertain Systems. *J. Syst. Sci. Complex.* **2018**, *31*, 4–21. [CrossRef]
32. Zhang, M.; Rosales, L.P.B.; Ortega, R.; Liu, Z.; Su, H. Pid, Passivity-Based Control of Port-Hamiltonian Systems. *IEEE Trans. Autom. Control* **2018**, *63*, 1032–1044. [CrossRef]
33. Mahto, T.; Mukherjee, V. Fractional Order Fuzzy PID Controller for Wind Energy-Based Hybrid Power System Using Quasi-Oppositional Harmony Search Algorithm. *IET Gener. Transm. Dis.* **2017**, *11*, 3299–3309. [CrossRef]
34. Gil, P.; Sebastião, A.; Lucena, C. Constrained Nonlinear-Based Optimisation Applied to Fuzzy PID Controllers Tuning. *Asian J. Control* **2018**, *20*, 135–148. [CrossRef]
35. Amirhossein, A.; Reza, S.; Ali, J. Performance and Robustness of Optimal Fractional Fuzzy PID Controllers for Pitch Control of a Wind Turbine Using Chaotic Optimization Algorithms. *ISA Trans.* **2018**, *79*, 27–44.

36. Mohan, V.; Chhabra, H.; Rani, A.; Singh, V. An Expert 2DOF Fractional Order Fuzzy PID Controller for Nonlinear Systems. *Neural Comput. Appl.* **2018**, 1–18. [CrossRef]
37. Vedrana, S.; Mate, J.; Baotić, M. Wind Turbine Power References in Coordinated Control of Wind Farms. *Autom. J. Control Meas. Electron. Comput. Commun.* **2011**, *52*, 82–94.
38. Barlas, T.K.; Kuik, G.A.M.V. Review of State of the Art in Smart Rotor Control Research for Wind Turbines. *Prog. Aerosp. Sci.* **2010**, *46*, 1–27. [CrossRef]
39. Jonkman, J.M.; Butterfield, S.; Musial, W.; Scott, G. *Definition of a 5-MW Reference Wind Turbine for Offshore System Development*; National Renewable Energy Lab.: Lakewood, CO, USA, 2009.
40. Grunnet, J.D.; Soltani, M.; Knudsen, T.; Kragelund, M.N.; Bak, T. Aeolus Toolbox for Dynamic Wind Farm Model, Simulation and Control. In Proceedings of the European Wind Energy Conference & Exhibition, Warsaw, Poland, 20–23 April 2010.
41. Pardalos, P.M.; Rebennack, S.; Pereira, M.V.F.; Iliadis, N.A.; Pappu, V. *Handbook of Wind Power Systems*; Springer: Berlin, Germany, 2014.
42. Soltani, M.N.; Knudsen, T.; Svenstrup, M.; Wisniewski, R.; Brath, P.; Ortega, R.; Johnson, K. Estimation of Rotor Effective Wind Speed: A Comparison. *IEEE Trans. Control Syst. Technol.* **2013**, *21*, 1155–1167. [CrossRef]
43. Manwell, J.F.; Mcgowan, J.G.; Rogers, A.L. *Wind Energy Explained: Theory, Design and Application*, 2nd ed.; John Wiley & Sons: Hoboken, NJ, USA, 2002.
44. Simley, E.; Dunne, F.; Laks, J.; Pao, L.Y. 10 Lidars and Wind Turbine Control—Part 2. DTU Wind Energy-E-Report-0029. Available online: http://citeseerx.ist.psu.edu/viewdoc/download;jsessionid=16F5DC8769E46EEC0A5834631C48C1E0?doi=10.1.1.361.2830&rep=rep1&type=pdf (accessed on 21 April 2019).
45. Luis, V.; Salvador, J. Quadratic programming. *J. Oper. Res. Soc.* **2013**, *16*, 256–257.
46. Cimini, G.; Bemporad, A. Exact Complexity Certification of Active-Set Methods for Quadratic Programming. *IEEE Trans. Autom. Control.* **2017**, *62*, 6094–6109. [CrossRef]
47. Bao, Y.; Xiong, T.; Hu, Z. PSO-MISMO Modeling Strategy for Multistep-Ahead Time Series Prediction. *IEEE Trans. Cybern.* **2014**, *44*, 655–668. [PubMed]
48. Nery, G.A., Jr.; Martins Márcio, A.F.; Kalid, R. A PSO-Based Optimal Tuning Strategy for Constrained Multivariable Predictive Controllers with Model Uncertainty. *ISA Trans.* **2014**, *53*, 560–567. [CrossRef]
49. Sahu, R.K.; Panda, S.; Chandra Sekhar, G.T. A Novel Hybrid PSO-PS Optimized Fuzzy PI Controller for AGC in Multi Area Interconnected Power Systems. *Int. J. Elec. Power* **2015**, *64*, 880–893. [CrossRef]
50. Gong, D.W.; Sun, J.; Miao, Z. A Set-Based Genetic Algorithm for Interval Many-Objective Optimization Problems. *IEEE Trans. Evol. Comput.* **2016**, *22*, 47–60. [CrossRef]
51. Buhl, M. *MCrunch User's Guide for Version 1.00*, 1st ed.; National Renewable Energy Laboratory: Lakewood, CO, USA, 2008.